

# A Monolithic Serial-Kinematic Nanopositioner With Integrated Sensors and Actuators

Steven Ian Moore, Meysam Omidbeike, Andrew Fleming, *Member, IEEE*, Yuen Kuan Yong, *Member, IEEE*

**Abstract**—This article describes the design, modeling and simulation of a serial-kinematic nanopositioner machined from a single sheet of piezoelectric material. In this class of nanopositioners, the flexures, sensors and actuators are completely integrated into a single monolithic structure. A non-trivial electrode topology is etched into the sheet to achieve in-plane bending and displacement of the moving platform. Finite element analysis predicts a sensitivity of 18.6 nm/V in the x-axis and 18.1 nm/V in the y-axis with a voltage limit of -250 V to 1000 V. The first resonance frequency is 250 Hz in the Z axis. This design enables high-speed, long-range, lateral positioning in space-limited applications.

## I. INTRODUCTION

Nanopositioners encompass a set of devices whose motion is controlled with nanometer resolution [1]. Nanopositioners enable the characterization and manipulation of matter at nanoscales and are a core technology in the nanotechnology field. Applications include atomic force microscopy [2]–[7], data storage [8], nanofabrication [9], [10], cell surgery [11], and precision optics [12].

The piezoelectric tube nanopositioner [13] exemplifies the first widely utilized nanopositioning system. These monolithic devices are easy to fabricate, and easily integrate into larger systems such as microscopes. However, with their maximum displacement range being a function of tube length, these tubes are unable to be miniaturized. In addition, the speed of the tube is limited by lateral resonances, and cross-coupling between the lateral and vertical directions limit their utility [14].

To address the performance limitations of the tube and other monolithic nanopositioning designs, flexure-based nanopositioners have been reported as an alternative [15]–[19]. High stiffnesses are achieved by fabricating the flexures from bulk metal which increases the bandwidth and reduces the cross-coupling compared to monolithic designs. Large piezoelectric stack actuators are required to drive the stiff flexures which requires the use of specialized amplifiers to handle significant electrical loads. This drastically increases the cost and size of flexure based nanopositioners.

To capture the advantages of both monolithic and flexure based nanopositioners, a new class of nanopositioning stages constructed from a single sheet of piezoelectric material has been reported [20]. Guiding flexures are etched into the structure with individual electrical control over each active flexure. They are the thinnest yet reported nanopositioning

stages with a thickness of within 500  $\mu\text{m}$  to 1.5 mm. This new class of nanopositioners will enable a new range of ultra-compact applications in scanning probe microscopy, scanning electron microscopy, and active optics.

This work proposes a new monolithic nanopositioner design with a serial-kinematic structure which provides several advantages over the parallel-kinematic design reported by [20]. One advantage is that the serial-kinematic flexures do not experience compression, which leads to increased range. A disadvantage is the increased mechanical and electrode complexity.

The remainder of the paper precedes as follows. Section II outlines the structural design, fabrication, and actuating principles of the nanopositioner. Section III models the static motion of a single flexure actuator which is employed in Section IV to produce a lumped model of the entire nanopositioner. Section V validates the static modeling of the nanopositioner and presents a model analysis of the design.

## II. DESIGN AND FABRICATION

Figure 1(a) shows the fabricated serial-kinematic nanopositioner where a smaller inner stage is nested into a larger outer stage. The nanopositioner is fabricated from a single square sheet of PZT-5H ceramic of thickness 500  $\mu\text{m}$ . The piezoelectric sheet is coated with a 5  $\mu\text{m}$  layer of nickel on both sides. The mechanical and electrode features are created by laser machining and surface ablation. Figure 1(c) shows the mechanical features and the nickel electrode arrangement with dimensions. The nickel layer on the reverse side is not etched.

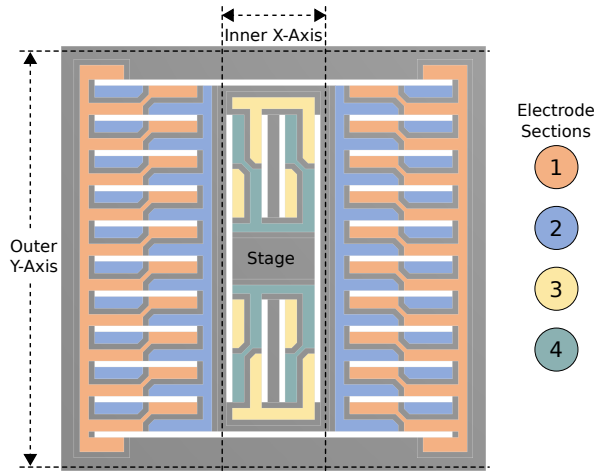
The motion of the X and Y axes are constrained by a set of thick flexures on either side of the stage. The flexures guide the nanopositioner in the compliant directions, and provide the mechanism for actuation. The inner x-axis is guided by 4 active flexures and two non-active flexures. The outer y-axis is guided by 20 active flexures.

The electrode over each active flexure is split into four quadrants as shown in Figure 2. Two sections are formed by electrically connecting the first and third quadrants for one section and the second and fourth for the other section. With the bottom electrode grounded, opposite voltages are applied to the two sectioned electrodes to create side-to-side motions. When actuators of a single axis are moved towards the same direction, translational motions are generated. When the actuators of each stage are moved in opposite directions, rotational motions are generated. Considering the complete nanopositioner, Figure 1(b) shows the electrode sections of the entire set of flexures to achieve translation in the X and

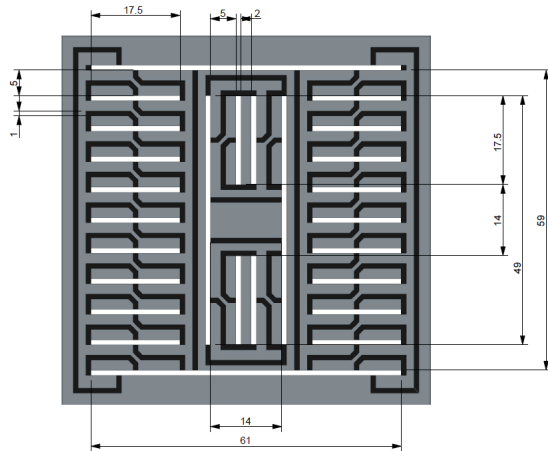
The authors are with the School of Electrical Engineering and Computer Science, the University of Newcastle, Australia. Email: steven.i.moore@uon.edu.au, meysam.omidbeike@uon.edu.au, andrew.fleming@newcastle.edu.au, yuenkuan.yong@newcastle.edu.au.



(a) The machined piezoelectric sheet forming the nanopositioner.



(b) The electrode sections of the nanopositioner for translation in the X and Y axes.



(c) The dimensions of the nanopositioner. Cutouts are shown in white, the nickel coating is shown in grey and the PZT-5H is shown in black.

Fig. 1. The nanopositioner design. (a) The photo of the prototype design. (b) Schematic of the piezoelectric electrode layout. (c) Schematic with the structural dimensions.

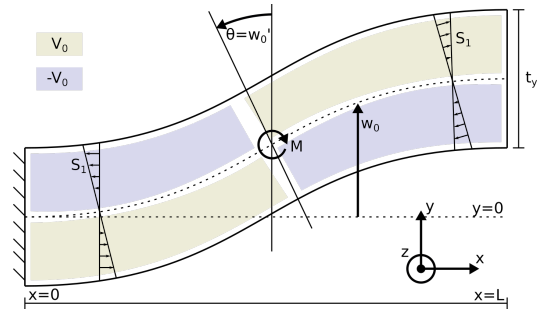


Fig. 2. The flexure has four electrodes on each quarter of the beam in the x-y plane. Two of the electrodes are actuated positively and the other two are actuated negatively. The diagram shows the positive orientation of a cross section's deflection  $w_0(x)$ , rotation  $w'_0(x)$ , and bending moment  $M(x)$ .

Y axes. The sections on each axis are driven with opposite polarity voltages, where sections 1 and 2 develop motion in the Y axis and sections 3 and 4 develop motion in the X axis.

### III. STATIC MODELING OF A FLEXURE

The constitutive equations of the piezoelectric material which forms the flexures relates the stress, strain, and electric field in the material. The electric field is a function of the applied voltages (the input), the strain is related to the deflection of the flexure (the output), and the stress in the flexure is quantified with an equilibrium condition. The modeling objective is to find the electric field-voltage relationship and the stress-displacement relationship, and finally use the constitutive equations and the equilibrium condition to find the voltage-deflection characteristic. A diagram of the flexure is shown in Figure 2.

a) *Stress-Displacement Relationship:* Euler-Bernoulli beam theory parameterizes the 3-dimensional displacement field in the flexure in terms of the 1-dimensional deflection of the flexure  $w_0$  [21]–[23]:

$$u_1(x, y, z) = -yw'_0(x), \quad (1)$$

$$u_2(x, y, z) = w_0(x), \quad (2)$$

$$u_3(x, y, z) = 0, \quad (3)$$

where  $(u_1, u_2, u_3)$  is the displacement of an infinitesimal piece of the flexure in the x-y-z-axes respectively, and the prime ( $'$ ) is the derivate with respect to  $x$ . The quantity  $w'_0$  is the angle of rotation of a cross-section of the flexure around the neutral axis. The displacement field indicates that: the displacement in the y-axis is solely due to the deflection of the flexure; there is no displacement in the z-axis; and displacement in the x-axis is due to rotation of a flexure cross-section. With the given displacement field above, there is only one non-zero component of the strain:

$$S_1(x, y, z) = u'_1 = -yw''_0. \quad (4)$$

b) *Electric Field-Voltage Relationship:* A parallel-plate capacitive structure is assumed to model the generated electric field. One-side of the flexure is grounded, and the other

is split into four electrodes distributed in the x-y-plane. The piezoelectric flexure is polarized along the z-axis. The electric field is:

$$E_3(x, y, z) = \frac{V(x, y)}{t_z}, \quad (5)$$

where  $t_z$  is the thickness of the flexure in the z-direction and the voltage is:

$$V(x, y) = \begin{cases} -V_0 & x < L/2, y > 0 \\ V_0 & x < L/2, y < 0 \\ V_0 & x > L/2, y > 0 \\ -V_0 & x > L/2, y < 0 \end{cases}, \quad (6)$$

where  $V_0$  is the input voltage.

*c) Constitutive Equations and the Bending Moment:*

An Euler-Bernoulli beam has only one non-zero stress and strain component, and the electric field is only applied in the direction of piezoelectric polarization. In this case, the constitutive equations of a linear piezoelectric material simplify to:

$$T_1 = c_{11}S_1 - e_{31}E_3, \quad (7)$$

$$D_3 = e_{31}S_1 + \epsilon_{33}E_3, \quad (8)$$

where  $T_1$  is the stress,  $D_3$  is the electric displacement,  $c_{11}$  is Young's modulus,  $e_{31}$  is the piezoelectric coefficient, and  $\epsilon_{33}$  is the permittivity. Substituting Equations (4) and (5) into Equation (7) allows the stress to be expressed in terms of the input voltage and output displacement as:

$$T_1(x, y, z) = -c_{11}yw_0''(x) - e_{31}\frac{V(x, y)}{t_z}. \quad (9)$$

Next consider a cross-sectional piece of the flexure. The stresses cause a moment to be applied to the cross-section causing it to rotate. The moment around the neutral axis of the flexure is:

$$M(x) = \int_A yT_1 dy dz, \quad (10)$$

where  $A$  is the domain of the cross-section, and the origin in the y-axis is the neutral plane along the center of the flexure. Substituting Equation (9) into the above equation and integrating results in:

$$M(x) = -c_{11}Iw_0''(x) - k_VV_0, \quad (11)$$

where the moment of inertia  $I$  and actuation gain  $k_V$  are:

$$I = t_z \int_{-t_y/2}^{t_y/2} y^2 dy = \frac{t_z t_y^3}{12}, \quad (12)$$

$$k_V = \begin{cases} e_{31} \int_0^{t_y/2} -y dy + \int_{-t_y/2}^0 y dy = -\frac{e_{31}t_y^2}{4} & x < L/2 \\ e_{31} \int_0^{t_y/2} y dy + \int_{-t_y/2}^0 -y dy = \frac{e_{31}t_y^2}{4} & x > L/2 \end{cases}, \quad (13)$$

$$= -\frac{e_{31}t_y^2}{4} \left(1 - 2h\left(x - \frac{L}{2}\right)\right), \quad (14)$$

where  $h(x)$  is the step function.

*d) Equilibrium and the Displacement Characteristic:*

When the flexure has settled to equilibrium, the net moment and net shear on each cross section is zero. With no externally applied shear force or bending moment, the internal bending moment on each cross section is zero, that is  $M(x) = 0$ . Applying this condition to Equation (11), making  $w_0''$  the subject and substituting in Equation (14) leads to the expression:

$$w_0''(x) = \frac{e_{31}t_y^2}{4c_{11}I} \left(1 - 2h\left(x - \frac{L}{2}\right)\right) V_0. \quad (15)$$

This expression is integrated once to get the angle of rotation of the cross-section, and integrated twice to get the deflection. The constants of integration are evaluated with the geometric boundary conditions  $w_0'(0) = 0$  and  $w_0(0) = 0$ . The rotation and deflection of the flexure are:

$$w_0'(x) = \frac{e_{31}t_y^2}{4c_{11}I} \left(x - 2\left(x - \frac{L}{2}\right)h\left(x - \frac{L}{2}\right)\right) V_0, \quad (16)$$

$$w_0(x) = \frac{e_{31}t_y^2}{4c_{11}I} \left(\frac{x^2}{2} - \left(x - \frac{L}{2}\right)^2 h\left(x - \frac{L}{2}\right)\right) V_0. \quad (17)$$

The expressions are evaluated at  $x = L$  to give the rotation and deflection at the tip of the flexure as a function of the input voltage:

$$w_0'(L) = 0, \quad (18)$$

$$w_0(L) = \frac{e_{31}t_y^2 L^2}{16c_{11}I} V_0. \quad (19)$$

#### IV. STATIC GAIN OF THE INNER AND OUTER STAGES

The model of the inner and outer axes are formed by considering each stage to be rigid with a set of lumped springs guiding it and force actuators driving it. The objective is to derive a one degree-of-freedom model of the flexures, that can easily be combined into a lumped model. This is achieved by parameterizing the motion of the flexure with one degree-of-freedom and deriving its characteristic equation with the principle of minimum potential energy. By equating the characteristic equation with Hooke's law, the effective stiffness and force of a flexure is obtained.

*a) One Degree-of-Freedom Flexure Model:* The enthalpy of the flexure is a combination of the total strain energy and electrical energy stored in the flexure [24]:

$$H = \frac{1}{2} \int_V T_1 S_1 - D_3 E_3 dV, \quad (20)$$

$$= \frac{1}{2} \int_0^L c_{11}I (w_0'')^2 + 2k_V V_0 w_0'' - \epsilon_{33} t_z t_y E_3^2 dx. \quad (21)$$

For a one degree-of-freedom system, the solution for the piezoelectric flexure's transverse deflection is assumed to be:

$$w_0(x) = q_0 W_0(x), \quad (22)$$

where  $q_0$  is the deflection at the end of the flexure, the one degree-of-freedom, and  $W_0(x)$  is the assumed spatial distribution of the transverse deflection. Substituting Equation (22)

TABLE I

PARAMETERS OF THE PIEZOELECTRIC FLEXURES FOR MODELING.

Description	Parameter	Value
Flexure Length (mm)	$L$	17.5
Flexure Thickness (mm)	$t_y$	5
Small Flexure Thickness (mm)	$\bar{t}_y$	2
Flexure Width (mm)	$t_z$	0.5
Elastic Modulus (GPa)	$c_{11}$	66
Density ( $kg/m^3$ )	$\rho$	7800
Piezoelectric Coefficient ( $C/m^2$ )	$e_{31}$	-10.92
Number of Inner Stage Flexures	$n_i$	4
Number of Small Inner Stage Flexures	$\bar{n}_i$	2
Number of Outer Stage Flexures	$n_o$	20

into Equation (21) allows the enthalpy to be expressed in terms of the degree-of-freedom  $q_0$ :

$$H = \frac{1}{2}k_e q_0^2 - f_e q_0 - \varepsilon_{33} t_y t_z E_3^2, \quad (23)$$

where the parameters  $k_e$  and  $f_e$  are given by:

$$k_e = \int_0^L c_{11} I (W_0'')^2 dx, \quad (24)$$

$$f_e = - \int_0^L k_V V_0 W_0'' dx. \quad (25)$$

The principle of minimum total potential energy states that the first variation of the enthalpy is zero [23]. The principle is applied to Equation (23) and is evaluated as:

$$0 = \delta H = (k_e q_0 - f_e) \delta q_0, \quad (26)$$

where  $\delta$  is the variational operator. This equation holds when:

$$k_e q_0 = f_e. \quad (27)$$

This characteristic equation of the one degree-of-freedom model matches Hooke's law making  $k_e$  the effective stiffness, and  $f_e$  the effective force of the flexure.

The spatial distribution  $W(x)$  of the deflection is chosen from the solution of the static deflection from Equation (17). It is scaled to ensure  $q_0$  is the tip deflection. The spatial distribution is:

$$W_0(x) = \frac{4}{L^2} \left( \frac{x^2}{2} - (x - \frac{L}{2})^2 h(x - \frac{L}{2}) \right). \quad (28)$$

With  $W_0(x)$  defined as above, Equations (24) and (25) are evaluated for the effective stiffness and force of a flexure as:

$$k_e = \frac{16c_{11}I}{L^3}, \quad (29)$$

$$f_e = \frac{e_{31}t_y^2}{L} V_0. \quad (30)$$

*b) Lumped Model of the Inner Stage:* The effective stiffness and force of the inner stage of the nanopositioner is:

$$k_{inner} = n_i k_e + \bar{n}_i \bar{k}_e, \quad (31)$$

$$f_{inner} = n_i f_e, \quad (32)$$

where  $n_i$  is the number of flexures connected to the stage. There are two smaller flexures connected to the inner stage

TABLE II

PIEZOELECTRIC PROPERTIES FOR THE PZT-5A BIMORPH SHEET FROM PIEZO SYSTEM INC.

Piezoelectric coefficient, $C/m^2$	
$e_{31}$	-10.92
$e_{33}$	12.08
$e_{15}$	12.29
Relative permittivity, $\varepsilon = \varepsilon^S / \varepsilon_o$	
$\varepsilon_{11}$	916
$\varepsilon_{33}$	830
Piezoelectric constant, $pm/V$	
$d_{31}$	-190

TABLE III

COMPARISON OF ANALYTICAL AND FEA STATIC GAINS.

Static gain (nm/V)	Analytical	ANSYS
Inner stage (x-axis)	14.7	18.6
Outer stage (y-axis)	15.2	18.1

which provide no actuation. Their number, thickness and effective stiffness are designated  $\bar{n}_i$ ,  $\bar{t}_y$ , and  $\bar{k}_e$ . With the parameters in Table I the gain of the inner axis is  $14.73 \text{ nm V}^{-1}$ .

*c) Lumped Model of the Outer Stage:* The effective stiffness and force of the outer stage is:

$$k_{outer} = n_o k_e \quad (33)$$

$$f_{outer} = n_o f_e \quad (34)$$

where  $n_o$  is the number of flexures connected to the outer stage. The gain of the outer stage with the parameters in Table I is  $15.20 \text{ nm V}^{-1}$ .

## V. FINITE-ELEMENT-ANALYSIS

A numerical finite-element (FE) model of the monolithic stage was constructed using ANSYS workbench. Displacement of all four edges of the stage are fixed as shown in Figure 3. The piezoelectric properties of the stage are modeled using the ANSYS Piezo and MEMS Application Customization Toolkit (ACT) extension. The piezoelectric properties for PZT-5A are listed in Table II. Each piezoelectric layer is polarized outwards along its thickness direction.

### A. Static gain

To obtain the displacement per unit voltage along the x and y axes, +1 V and -1 V is applied to the electrodes in orange and blue respectively as shown in Figure 3. The corresponding displacement is shown in the same figure. The static gain of the inner (x-axis) and outer (y-axis) platform is  $18.6 \text{ nm/V}$  and  $18.1 \text{ nm/V}$  respectively. The breakdown electric field strength of PZT5H is  $-500 \text{ V mm}^{-1}$  to  $2 \text{ kV mm}^{-1}$  allowing for a voltage of -250 V to 1000 V to be applied. Therefore the range of the nanopositioner is  $23.250 \mu\text{m}$  in the x-axis and  $22.625 \mu\text{m}$  in the y-axis. Table III compares the analytical and ANSYS results for the static gains, which are in close agreement.

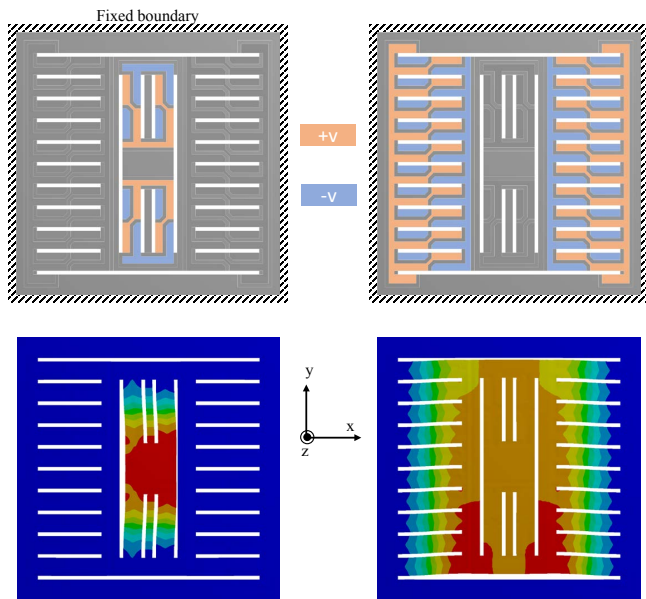


Fig. 3. Simulated displacement along the x and y axes when +1 V is applied to the electrodes in orange and -1 V is applied to the electrodes in blue.

### B. Resonance frequencies

The resonance frequencies of the stage were simulated using the modal analysis module of ANSYS. The first four modes are shown in Figure 4(a)-(d). The first resonant mode is the out-of-plane mode along the z-axis which appears at 249 Hz.

To search for the lateral modes along the x and y axes of the stage, the out-of-plane motions along the z-axis were constrained. Figures 4(e) and 4(f) show the lateral modes of the stage. The lateral resonance frequencies appear at 5243.3 Hz and 5225.2 Hz along the x and y axes respectively.

## VI. EXPERIMENTAL RESULTS

Preliminary experimental work characterizes the lateral displacement of the nanopositioner and x-y-z frequency response under lateral actuation. Frequency responses were measured with a Polytec MSA-100-3D laser vibrometer, and displacement responses were measured with an Attocube FPS3010 interferometer.

Figure 5 shows the displacement in the inner x-axis and outer y-axis under the corresponding lateral actuation. For a  $\pm 200$  V input voltage, the inner x-axis displaced by  $10.08 \mu\text{m}$  and the outer y-axis displacement by  $10.45 \mu\text{m}$ . The per volt static gains of the stage are  $25.2 \text{ nm/V}$  and  $26.1 \text{ nm/V}$  for the x and y axes respectively. These gains are higher than predicted due to uncertainty in the piezoelectric coefficient. In addition, Figure 5 shows the typical hysteresis non-linearity associated with piezoelectric actuators. This is caused by the applied voltage altering the polarization of the piezoelectric material. This non-linearity, while expected, is not modeled by the linear constitutive equations used to model the stage.

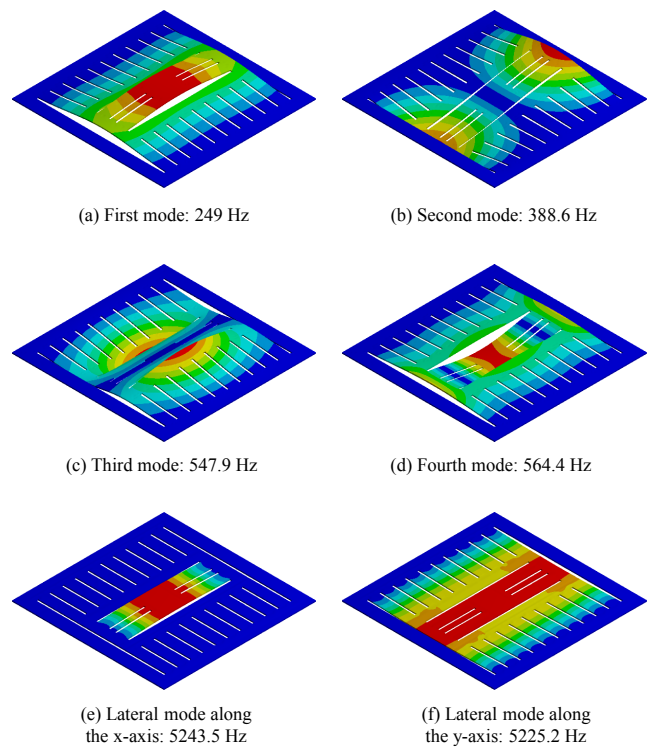


Fig. 4. Simulated resonance frequencies of the serial-kinematic planar stage.

Figure 6 shows the displacement frequency response in the range 100 Hz to 1 kHz. The lateral motion exhibits no dynamics in this range as expected while a number of resonances are observed in the out-of-plane z-axis motion. The largest peaks in the frequency responses match the FE modal analysis from the FEA (Figure 4). The additional smaller modes are associated with coupling between the stage and the metal frame it is mounted in.

## VII. CONCLUSIONS

The monolithic construction of the nanopositioner simplifies fabrication making it accessible to many cost sensitive applications. Fabricated from a thin piezoelectric sheet, the nanopositioner is well suited to ultra-compact designs. The flexure based design pushes the lateral resonance frequencies to much higher frequencies compared to tube based nanopositioners. And compared to other flexure based designs, the size of the electrical load is significantly reduced. Compared to the previous reported parallel-kinematic nanopositioner, the serial-kinematic design extends the range and reduces the cross coupling.

The authors are currently experimentally characterizing the nanopositioner, developing feedback control strategies for precision motion control, and refining the instrumentation methods employed with the nanopositioner.

## REFERENCES

- [1] A. J. Fleming and K. K. Leang, *Design, Modeling and Control of Nanopositioning Systems*. London, UK: Springer, 2014.

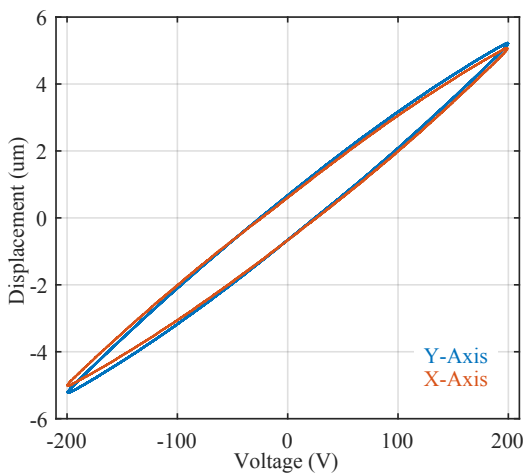


Fig. 5. The displacement of the nanopositioner in the x- and y-axis under lateral actuation in the inner x-direction and outer y-direction.

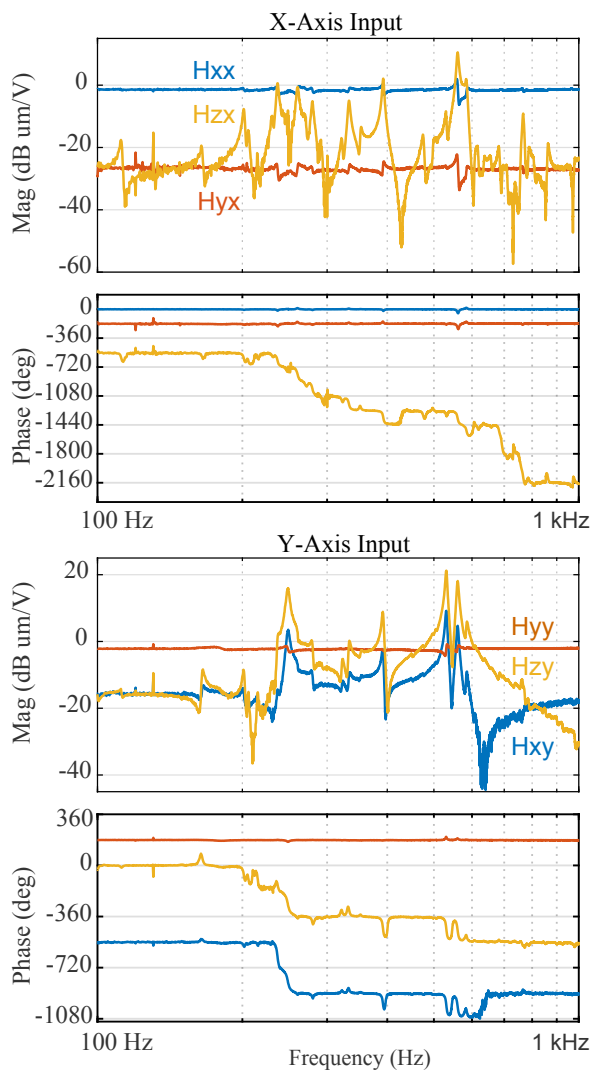


Fig. 6. The frequency response of the stage in the x-y-z axes under lateral actuation in the inner x-direction and outer y-direction. The reference voltage is amplified by a gain of 50 before actuating the stage.

- [2] M. S. Rana, H. R. Pota, and I. R. Petersen, "Performance of sinusoidal scanning with mpc in afm imaging," *IEEE/ASME Transactions on Mechatronics*, vol. 20, no. 1, pp. 73–83, Feb 2015.
- [3] A. Bazaeei, Y. K. Yong, and R. Moheimani, "Combining spiral scanning and internal model control for sequential afm imaging at video rate," *IEEE/ASME Transactions on Mechatronics*, 2016.
- [4] S. M. Salapaka and M. V. Salapaka, "Scanning probe microscopy," *IEEE Control Systems*, vol. 28, no. 2, pp. 65–83, April 2008.
- [5] D. Y. Abramovitch, S. B. Andersson, L. Y. Pao, and G. Schitter, "A tutorial on the mechanisms, dynamics, and control of atomic force microscopes," in *Proc. American Control Conference*, New York City, NY, July 2007, pp. 3488–3502.
- [6] A. J. Fleming, B. J. Kenton, and K. K. Leang, "Bridging the gap between conventional and video-speed scanning probe microscopes," *Ultramicroscopy*, vol. 110, no. 9, pp. 1205–1214, August 2010.
- [7] M. Fairbairn, S. O. R. Moheimani, and A. J. Fleming, "Q control of an atomic force microscope micro-cantilever: a sensor-less approach," *IEEE/ASME Journal of Microelectromechanical Systems*, vol. 20, no. 6, pp. 1372–1381, December 2011.
- [8] A. Sebastian, A. Pantazi, H. Pozidis, and E. Elefthriou, "Nanopositioning for probe-based data storage," *IEEE Control Systems*, vol. 28, no. 4, pp. 26–35, August 2008.
- [9] S. Mishra, J. Coaplen, and M. Tomizuka, "Precision positioning of wafer scanners. segmented iterative learning control for nonrepetitive disturbances," *IEEE Control Systems*, vol. 27, no. 4, pp. 20–25, August 2007.
- [10] A. Ferreira and C. Mavroidis, "Virtual reality and haptics for nanorobotics," *IEEE Robotics and Automation Magazine*, vol. 13, no. 3, pp. 78–92, September 2006.
- [11] Z.-Q. Fan, X.-W. Li, Y. Liu, Q.-G. Meng, Y.-P. Wang, Y.-P. Hou, G.-B. Zhou, and S.-E. Zhu, "Piezo-assisted in vitro fertilization of mouse oocytes with spermatozoa retrieved from epididymides stored at 4 degree c," *The Journal of Reproduction and Development*, vol. 54, no. 2, pp. 107–112, 2008.
- [12] S. Z. S. Hassen, M. Heurs, E. H. Huntington, I. R. Petersen, and M. R. James, "Frequency locking of an optical cavity using linearquadratic gaussian integral control," *Journal of Physics B: Atomic, Molecular and Optical Physics*, vol. 42, no. 17, p. 175501, 2009.
- [13] G. Binnig and D. P. E. Smith, "Single-tube three-dimensional scanner for scanning tunneling microscopy," *Review of Scientific Instruments*, vol. 57, no. 8, pp. 1688–1689, August 1986.
- [14] J. Maess, A. J. Fleming, and F. Allgöwer, "Simulation of dynamics-coupling in piezoelectric tube scanners by reduced order finite element models," *Review of Scientific Instruments*, vol. 79, pp. 015 105(1–9), January 2008.
- [15] H. Tang and Y. Li, "A new flexure-based  $y\theta$  nanomanipulator with nanometer-scale resolution and millimeter-scale workspace," *IEEE/ASME Transactions on Mechatronics*, vol. 20, no. 3, pp. 1320–1330, June 2015.
- [16] K. W. Chae, W.-B. Kim, and Y. H. Jeong, "A transparent polymeric flexure-hinge nanopositioner, actuated by a piezoelectric stack actuator," *Nanotechnology*, vol. 22, no. 33, p. 335501, 2011.
- [17] L. L. Howell, *Compliant mechanisms*. New York, New York: John Wiley and Sons, 2000.
- [18] B. J. Kenton, A. J. Fleming, and K. K. Leang, "A compact ultra-fast vertical nanopositioner for improving SPM scan speed," *Review of Scientific Instruments*, vol. 82, no. 12, pp. 123 703(1–8), 2011.
- [19] Y. K. Yong, S. O. R. Moheimani, B. J. Kenton, and K. K. Leang, "Invited review article: High-speed flexure-guided nanopositioning: Mechanical design and control issues," *Review of Scientific Instruments*, vol. 83, no. 12, p. 121101, 2012.
- [20] A. J. Fleming and Y. K. Yong, "An ultra-thin monolithic xy nanopositioning stage constructed from a single sheet of piezoelectric material," *IEEE/ASME Transactions on Mechatronics*, vol. 22, no. 6, pp. 2611–2618, 2017.
- [21] G. R. Cowper, "The shear coefficient in timoshenko's beam theory," *Journal of Applied Mechanics*, vol. 33, no. 2, pp. 335–340, 1966.
- [22] V. Piefort, "Finite element modelling of piezoelectric active structures," Ph.D. dissertation, Université Libre de Bruxelles, 2001.
- [23] J. N. Reddy, *Energy Principles and Variational Methods in Applied Mechanics*. John Wiley & Sons, 2002.
- [24] A. Preumont, *Vibration Control of Active Structures*. Springer Netherlands, 2011.